Kent Academic Repository

Moscadelli, L., Beuther, H., Sanna, A., Beltrán, M. T., Gieser, C., Henning, Th., Klaassen, P. D., Kuiper, R., Leurini, S., Möller, T. and others (2026) *Protostellar Outflows at the EarliesT Stages (POETS). IX.Magnetohydrodynamic disk winds traced by SO and SO2 in luminous protostars.* Astronomy & Astrophysics, 711 . ISSN 0004-6361.

Downloaded from

https://kar.kent.ac.uk/115592/ The University of Kent's Academic Repository KAR

The version of record is available from

https://doi.org/10.1051/0004-6361/202660059

This document version

Publisher pdf

DOI for this version

Licence for this version

CC BY (Attribution)

Additional information

Versions of research works

Versions of Record

If this version is the version of record, it is the same as the published version available on the publisher's web site. Cite as the published version.

Author Accepted Manuscripts

If this document is identified as the Author Accepted Manuscript it is the version after peer review but before type setting, copy editing or publisher branding. Cite as Surname, Initial. (Year) 'Title of article'. To be published in ***Title of Journal*** , Volume and issue numbers [peer-reviewed accepted version]. Available at: DOI or URL (Accessed: date).

Enquiries

If you have questions about this document contact ResearchSupport@kent.ac.uk. Please include the URL of the record in KAR. If you believe that your, or a third party's rights have been compromised through this document please see our Take Down policy (available from https://www.kent.ac.uk/guides/kar-the-kent-academic-repository#policies).

A&A, 711, A182 (2026)
https://doi.org/10.1051/0004-6361/202660059
© The Authors 2026

Astronomy & Astrophysics

Protostellar Outflows at the EarliesT Stages (POETS)

IX. Magnetohydrodynamic disk winds traced by SO and SO_2 in luminous protostars

L. Moscadelli[1,⋆], H. Beuther[2], A. Sanna[3], M. T. Beltrán[1], C. Gieser[2], Th. Henning[2], P. D. Klaassen[4], R. Kuiper[5], S. Leurini[3], T. Möller[6], A. Palau[7], R. E. Pudritz[8], Á. Sánchez-Monge[9,10], D. Semenov[11,2], J. S. Urquhart[12], and H. Zinnecker[13]

[1] INAF – Osservatorio Astrofisico di Arcetri, Largo E. Fermi 5, 50125 Firenze, Italy
[2] Max-Planck-Institut für Astronomie, Königstuhl 17, 69117 Heidelberg, Germany
[3] INAF – Osservatorio Astronomico di Cagliari, Via della Scienza 5, 09047 Selargius (CA), Italy
[4] UK Astronomy Technology Centre, Royal Observatory Edinburgh, Blackford Hill, Edinburgh, EH9 3HJ, UK
[5] Faculty of Physics, University of Duisburg-Essen, Lotharstraße 1, 47057 Duisburg, Germany
[6] I. Physikalisches Institut, Universität zu Köln, Zülpicher Str. 77, 50937 Köln, Germany
[7] Universidad Nacional Autónoma de México, Instituto de Radioastronomía y Astrofísica, Antigua Carretera a Pátzcuaro 8701, Ex-Hda. San José de la Huerta, 58089 Morelia, Michoacán, Mexico
[8] Department of Physics and Astronomy, McMaster University, 1280 Main St. W, Hamilton, ON L8S 4K1, Canada
[9] Institut de Ciències de l'Espai (ICE), CSIC, Campus UAB, Carrer de Can Magrans s/n, 08193 Bellaterra, Barcelona, Spain
[10] Institut d'Estudis Espacials de Catalunya (IEEC), 08860 Castelldefels, Barcelona, Spain
[11] Zentrum für Astronomie der Universität Heidelberg, Institut für Theoretische Astrophysik, Albert-Ueberle-Str. 2, 69120 Heidelberg, Germany
[12] Centre for Astrophysics and Planetary Science, University of Kent, Canterbury, CT2 7NH, UK
[13] Universidad Autónoma de Chile, Nucleo Astroquimica y Astrofisica, Avda Pedro de Valdivia 425, Providencia, Santiago de Chile, Chile

Received 25 March 2026 / Accepted 30 May 2026

ABSTRACT

Context. Magnetohydrodynamic (MHD) disk winds (DWs) can be responsible for removing angular momentum from the accretion disks of protostars, for driving mass accretion and disk evolution and dispersal, and, ultimately, for setting the conditions for planet formation.

Aims. We want to investigate two massive young stellar objects (YSOs), IRAS 21078+5211 and G035.02+0.35, where evidence for MHD DWs has been previously obtained at scales of 10–100 au through measurements of the 22 GHz water maser velocity distribution within the Protostellar Outflows at the EarliesT Stages survey. The different mass, 5.6±2 $M_\odot$ and ≈20 $M_\odot$, of the two YSOs allows us to investigate the dependence of MHD DWs on the YSO environment, too.

Methods. We employed IRAM Northern Extended Millimeter Array and archival Atacama Large Millimeter Array observations of IRAS 21078+5211 and G035.02+0.35, respectively, to study the gas kinematics and physical conditions of the corresponding protostellar winds on scales of 100–1000 au using the same molecular tracers.

Results. In IRAS 21078+5211, the emissions of several molecules, particularly SO, SO_2, CH_3CN, and CH_3OH, are distributed along the axis of the previously identified radio jet, and present a local standard of rest velocity (V_{LSR}) gradient transversal to the jet axis. Position-velocity (PV) plots of the SO lines show patterns consistent with Keplerian rotation. The SO_2 emission comes from high-velocity gas flowing close to the jet axis, while CH_3CN and CH_3OH present a larger radial extension than the S-bearing species. In G035.02+0.35, the same molecules are instead distributed along the (sky-projected) major axis of the rotating disk reported previously, and their V_{LSR} gradients consistently trace the disk rotation. The corresponding PV plots present Keplerian profiles. SO is the only molecular species whose emission extends well outside the disk. Our analysis shows that, in both YSOs, the spatial and velocity distributions of SO are consistent with a rotating wind magneto-centrifugally launched from the YSO disk. The comparison with models of molecule formation and excitation in shocks indicates that the different radial extension of the molecular species observed in the protostellar wind of IRAS 21078+5211, as well as the lack of molecules, except SO, in the G035.02+0.35's wind, can be well explained in terms of a radially extended MHD DW, rather than a compact X-wind.

Conclusions. This study provides compelling evidence that the SO and SO_2 emissions can be used to trace MHD DWs in luminous YSOs at scales of 100–1000 au, and confirms the results derived with water masers at scales of 10–100 au.

Key words. masers – techniques: interferometric – stars: formation – ISM: jets and outflows – ISM: kinematics and dynamics

⋆ Corresponding author: luca.moscadelli@inaf.it

Open Access article, published by EDP Sciences, under the terms of the Creative Commons Attribution License (https://creativecommons.org/licenses/by/4.0), which permits unrestricted use, distribution, and reproduction in any medium, provided the original work is properly cited.
This article is published in open access under the Subscribe to Open model. Subscribe to A&A to support open access publication.

1. Introduction

The removal of angular momentum is key to allow the surrounding gas to accrete onto the forming star. In an accretion disk, the transport of angular momentum can be driven either by turbulent (Shakura & Sunyaev 1973; Lynden-Bell & Pringle 1974) or magnetic (Pelletier & Pudritz 1992; Königl & Pudritz 2000) stresses. Recent advances in theory (Pudritz et al. 2025) and observations (Moscadelli et al. 2022; Pascucci et al. 2023; De Simone et al. 2024; Narang et al. 2026) favor models of magnetohydrodynamic (MHD) disk winds (DWs; Blandford & Payne 1982; Pudritz et al. 2007), since they can supersede magnetic turbulence and extract disk angular momentum in regions of low ionization, and also account for the commonly observed protostellar outflows, in the form of both slow and poorly collimated winds and fast jets. In this regard, the magneto-centrifugal acceleration of the wind can take place either at the interface of the stellar magnetosphere with the disk (X-winds; Shu et al. 1994), or from the whole centrifugally supported part of the disk (DW). While X-winds remove angular momentum only from the innermost disk radii, DWs remove angular momentum across an extended portion of the disk, and therefore they are able to extract from the disk a much larger amount of angular momentum. This distinction between X-wind and DW is essential to understand the wind's role in driving mass accretion and disk evolution and dispersal, and, ultimately, setting the conditions for planet formation (Kadam et al. 2025).

By measuring three-dimensional (3D) velocities and achieving linear resolutions of $\lesssim$1 au, very long baseline interferometry (VLBI) observations of 22 GHz water masers can directly trace the velocity field of protostellar winds (Moscadelli et al. 2007; Sanna et al. 2010; Moscadelli et al. 2011). The Protostellar Outflows at the EarliesT Stages (POETS; Moscadelli et al. 2016; Sanna et al. 2018; Moscadelli et al. 2019b) survey has studied the launching region of protostellar winds in a sample ($\approx$40) of luminous young stellar objects (YSOs) at linear resolutions of 1–100 au by means of VLBI water maser and Jansky Very Large Array (JVLA) continuum observations.

One of the most interesting results from POETS is that the distribution of the 3D maser velocities within a few 100 au from the YSOs can be generally interpreted in terms of MHD DWs. There are two kinds of prevalent maser kinematic configurations: (1) water maser positions and 3D velocities are collimated and trace a fast rotating jet, as in IRAS 21078+5211 (a.k.a. G092.69+3.08, Moscadelli et al. 2016, see their Fig. 8); and (2) the local standard of rest (LSR) velocity ($V_{\rm LSR}$) gradient of the water masers agrees with that of the underlying rotating disk (observed in thermal lines) and the proper motions point away from the disk midplane at large angles, as in G011.92−0.61 and G035.02+0.35 (Moscadelli et al. 2019b, see their Figs. 1 and 2, respectively). In (1) the water masers trace the fastest and most collimated portion of the MHD DW only (i.e., the jet); in (2) they mainly trace the slower and less collimated DW. If the disk is seen sufficiently close to edge-on, the $V_{\rm LSR}$ would reflect mainly the disk rotation, while the proper motions would be dominated by the poloidal velocities of the wind.

It is fundamental to test the MHD DW interpretation based on water maser VLBI at scales of 10–100 au through interferometric observations of thermal tracers at scales of 100–1000 au. Toward G011.92−0.61, the case of a MHD DW has been fully confirmed by our Atacama Large Millimeter Array (ALMA) 1.3 mm observations at a linear resolution of $\approx$100 au (Bayandina et al. 2025). The dust and molecular line (e.g., CH_3CN and CH_3OH) emissions of the rotating disk are well resolved and a strong collimated outflow is traced in SO and SO_2 lines up to a distance of $\approx$3400 au. The SO and SO_2 emissions show a rotation-dominated velocity pattern, a constant specific angular momentum, and a Keplerian profile that is consistent with a magneto-centrifugal DW origin with launching radii of 50–100 au.

Table 1. Properties of the studied YSOs.

Name	Distance (kpc)	Luminosity ($L_\odot$)	Mass ($M_\odot$)	Ref.
IRAS 21078+5211	1.63±0.05	5×10^3	5.6±2	1, 2, 3
G035.02+0.35	2.33±0.22	$1–3\times10^4$	$\approx$20	4, 5, 6

Notes. (1) Xu et al. (2013); (2) Moscadelli et al. (2016); (3) Moscadelli et al. (2021); (4) Wu et al. (2014); (5) Beltrán et al. (2014); (6) Olguin et al. (2026).

The goal of this article is to further test the water maser MHD DW predictions focusing on the YSOs IRAS 21078+5211 and G035.02+0.35, representative of the two characteristic maser kinematic configurations observed in POETS. The main properties of the two YSOs are listed in Table 1. The presence of a rotating molecular disk has been established in both IRAS 21078+5211, using IRAM Northern Extended Millimeter Array (NOEMA) observations at a linear resolution of $\approx$600 au (Moscadelli et al. 2021), and G035.02+0.35, employing ALMA Cycle 0 data at a linear resolution of $\approx$1000 au (Beltrán et al. 2014). While IRAS 21078+5211 emits a compact ($\lesssim$1000 au) radio jet powering a collimated molecular outflow (traced with SO emission at scales from 10^3 to 10^4 au), G035.02+0.35 is associated with an extended nonthermal jet, marked by a collimated chain of radio knots up to distances of 10^4 au (Sanna et al. 2019b).

Although the previous millimeter interferometric observations of IRAS 21078+5211 and G035.02+0.35 revealed the YSO disk-jet system, the linear resolution was not sufficient to constrain the wind launching mechanism. IRAS 21078+5211 has been recently reobserved with NOEMA at 1.3 mm using long baselines within the large program CORE (PI: H. Beuther, Beuther et al. 2018; Gieser et al. 2021; Ahmadi et al. 2023); for G035.02+0.35, ALMA Cycle 4 Band 6 archival observations are available. These two interferometric datasets overlap in frequency, and provide comparable linear ($\approx$250 au at the target distance) and velocity ($\approx$0.5 km s^{-1}) resolutions, which is optimal for a comparison of the gas kinematics between the two sources. The diverse wind kinematics observed with the water masers at scales of 10–100 au could reflect the different mass (and environment) of the two YSOs (see Table 1). It is therefore particularly interesting to also compare the wind properties at larger scales, to learn how they change with the YSO mass (and environment).

The structure of the article is as follows. Section 2 describes the NOEMA and ALMA observations. Section 3 presents the images of the structure and kinematics of the molecular disk and/or protostellar wind, and determines the gas physical conditions. In Sect. 4 the launching mechanism of the protostellar winds is discussed, highlighting similarities and differences between the two YSOs. Finally, our conclusions are presented in Sect. 5.

2. Observations

2.1. NOEMA observations

IRAS 21078+5211 (tracking center: RA(J2000) = $21^h\,09^m\,21\overset{s}{.}64$, Dec(J2000) = +52° 22′ 37.″5) was observed with the new long baselines in the new A configuration at NOEMA during the winter term 2022–2023 in three tracks between February 25 and March 4, 2023, in project W22AL003 (PI: H. Beuther). The covered baseline range was between ≈58 and ≈1690 m. The quasars 2013+370 and MWC349 were employed for bandpass and flux calibration, respectively. Gain calibration was performed via regularly interleaved observations of the quasars 2037+511 and 2022+542. The spectral coverage in the 1.3 mm band in the lower and upper sidebands was between ≈213.85 to ≈221.60 GHz and ≈229.37 to ≈237.17 GHz, respectively. The spectral resolution of 0.25 MHz corresponds at 220 GHz to a nominal velocity resolution of ≈0.34 km s^{-1}. In our data reduction we employed a uniform spectral resolution of 0.5 km s^{-1}. The assumed nominal $V_{\rm LSR}$ of the region is −6.1 km s^{-1}.

Calibration and imaging of the data was conducted within the GILDAS framework[1] with Clic and Mapping. By excluding strong line emission and combining the lower and upper sideband data, we obtained a double-sideband (DSB) continuum dataset for further imaging. The continuum data were self-calibrated within Mapping in phase-only in three loops with decreasing integration times of 300, 150 and 45 s. Imaging was then conducted in uniform weighting to achieve the highest spatial resolution. The final DSB continuum images have a synthesized beam with full width at half maximum (FWHM) major and minor sizes of 0.″193 × 0.″103 and a position angle (PA) of −173°. The continuum 1σ root mean square (rms) noise is 0.09 mJy beam^{-1}.

While the self-calibration improved the continuum data significantly with an increase in the signal-to-noise ratio of the maps from 19 to 136, no clear improvement of the line data was recognizable after applying the gain solutions from the continuum phase self-calibration. Therefore, for the spectral lines, we used the non-self-calibrated data products. The rms noise in 0.5 km s^{-1} channels is typically a few milliJansky per beam (or a few Kelvin in brightness temperature), with a synthesized beam comparable to the continuum data as described above.

2.2. ALMA archive data

G035.02+0.35 (tracking center: RA(J2000) = $18^h\,54^m\,00\overset{s}{.}6485$, Dec(J2000) = +02° 01′ 19.″278) was observed within the project 2016.1.01036.S (PI: P. Sanhueza) by ALMA in Cycle 4 on September 12, 2017, employing the extended configuration (C40-8). The phase calibrator was the quasar J1851+0035. 43 antennae of the 12 m Array took part to the observations covering baselines from ≈92 m to ≈8548 m. Four spectral windows (SPWs) that had a width of 1875 MHz centered at the sky frequency of 217.812, 220.013, 232.013, and 234.513 GHz were recorded. The correlator spectral channels were 1920 for the SPWs centered at 232.013 and 234.513 GHz, and 3840 for the SPWs centered at 217.812 and 220.013 GHz, providing a maximum velocity resolution of 0.67 km s^{-1}.

The restoring calibration employed the ALMA pipeline version 42254 of the Common Astronomy Software Applications (CASA; CASA Team 2022) package, version 5.4.0-70. The image of each SPW (continuum plus line emission) was produced manually using the TCLEAN task, using Hogbom deconvolution (Högbom 1974) and Briggs weighting (Briggs 1995), with the robust parameter set to 0.5 as a compromise between resolution and sensitivity to extended emission. The clean beams of the resulting images have FWHM major and minor sizes varying in the range 0.″12–0.″14 and 0.″09–0.″11, and PA in the range [−67°, −79°].

For each SPW, to determine the continuum level of the spectra and subtract it from the line emission, we used STATCONT (Sánchez-Monge et al. 2018), a statistical method of estimating the continuum level at each position of the map from the spectral distribution of the intensity at that position. Taking the average of the four SPWs, the 1.3 mm continuum image of G035.02+0.35 has a 1σ rms noise level of 0.32 mJy beam^{-1}. The 1σ rms noise in a single spectral channel varies in the interval 3–4.5 mJy beam^{-1} (or 5–8 K in brightness temperature), depending on the considered SPW.

3. Results

3.1. Structure and kinematics

Table 2 lists the main molecular lines we considered to determine the gas kinematics and physical conditions. Most of them are covered by both the NOEMA IRAS 21078+5211 and the ALMA G035.02+0.35 observational setups, which allows us to investigate the two sources by employing the same molecular tracers. To study the kinematics, we surveyed the spectral images and selected the molecular lines that satisfy two conditions: (1) being sufficiently intense to map an extended velocity range; (2) being representative of well-defined kinematic structures. Our choice includes typical tracers of massive disks, such as CH_3CN and CH_3OH (Cesaroni et al. 1999; Beltrán et al. 2004; Moscadelli et al. 2019a; Sanna et al. 2019a), and protostellar winds in low- and high-mass YSOs, such as SO and SO_2 (Tabone et al. 2017; Bayandina et al. 2025). For completeness, we note that the SiO 5–4 emission, another potential outflow tracer, is resolved out at these small scales.

Figure 1 presents the structure and kinematics of the gas traced by the SO 6_5–5_4 line in both targets. In IRAS 21078+5211 the SO emission extends over ≈1500 au in the jet direction at PA ≈ 50° (Moscadelli et al. 2024), marked by both the double-lobe JVLA C-band emission and the collimated proper motions of the water masers, and presents a well-defined $V_{\rm LSR}$ gradient transversal to the jet axis and parallel to the disk midplane (the dashed black line in Fig. 1a, lower plot). The $V_{\rm LSR}$ pattern of the SO emission in G035.02+0.35 is more complex, but the loci of maximum and minimum $V_{\rm LSR}$ define a direction for the $V_{\rm LSR}$ gradient (marked by the dotted black line in Fig. 1b, lower plot) that is roughly parallel to the (sky-projected) major axis (the dashed black line in Fig. 1b, lower plot) of the rotating molecular disk at PA ≈150° (Beltrán et al. 2014). The same direction corresponds also to the elongation of the radio continuum and the $V_{\rm LSR}$ gradient traced by the water masers (Moscadelli et al. 2019b, see their Fig. 2). It is interesting to note that the SO $V_{\rm LSR}$ gradient is slightly offset to the southwest with respect to the radio continuum and water maser distribution. While the core of the SO emission is well aligned with the 1.3 mm continuum, more diffuse SO emission extends beyond the 1.3 mm continuum to the northeast and protrudes in spurs oriented in a direction approximately parallel to the disk rotation axis (see Fig. 1b, upper plot).

Figures 2 and 3 compare the spatial distribution and kinematics of dust and gas at scales of 100–1000 au in IRAS 21078+5211 and G035.02+0.35 employing the same tracers. The gas

[1] http://www.iram.fr/IRAMFR/GILDAS

Table 2. Molecular lines employed in the analysis.

Frequency (GHz)	Molecule	Transition	E_u/k_B (K)
214.35704	SO	7_8–7_7	81
215.22065	SO	5_5–4_4	44
219.94944	SO	6_5–5_4	35
236.45229	SO	1_2–2_1	16
214.68938	SO_2	$16_{3,13}$–$16_{2,14}$	148
214.72829	SO_2	$17_{6,12}$–$18_{5,13}$	229
216.64330	SO_2	$22_{2,20}$–$22_{1,21}$	248
219.27598	SO_2	$22_{7,15}$–$23_{6,18}$	353
234.18705	SO_2	$28_{3,25}$–$28_{2,26}$	403
234.42159	SO_2	$16_{6,10}$–$17_{5,13}$	213
235.15172	SO_2	$4_{2,2}$–$3_{1,3}$	19
236.21669	SO_2	$16_{1,15}$–$15_{2,14}$	131
237.06883	SO_2	$12_{3,9}$–$12_{2,10}$	94
220.40390	CH_3CN	12_9–11_9	647
220.47581	CH_3CN	12_8–11_8	526
220.53932	CH_3CN	12_7–11_7	419
220.59442	CH_3CN	12_6–11_6	326
220.64108	CH_3CN	12_5–11_5	247
220.67929	CH_3CN	12_4–11_4	183
220.70902	CH_3CN	12_3–11_3	133
220.73026	CH_3CN	12_2–11_2	97
220.74301	CH_3CN	12_1–11_1	76
220.74726	CH_3CN	12_0–11_0	69
217.88650	CH_3OH	$20_{-1,19}$–$20_{0,20}$ E, $v_t = 0$	508
218.44006	CH_3OH	$4_{-2,3}$–$3_{-1,2}$ E, $v_t = 0$	45
220.07856	CH_3OH	$8_{0,8}$–$7_{-1,6}$ E, $v_t = 0$	97
221.29453	CH_3OH	$3_{2,1}$–$2_{-2,1}$ E, $v_t = 0$	40
229.58906	CH_3OH	$15_{-4,11}$–$16_{-3,14}$ E, $v_t = 0$	374
229.86412	CH_3OH	$19_{5,15}$–$20_{4,16}$ A, $v_t = 0$	579
230.02705	CH_3OH	$3_{2,1}$–$4_{1,4}$ E, $v_t = 0$	40
231.28111	CH_3OH	$10_{2,9}$–$9_{3,6}$ A, $v_t = 0$	165
232.41852	CH_3OH	$10_{2,8}$–$9_{3,7}$ A, $v_t = 0$	165
232.78345	CH_3OH	$18_{3,16}$–$17_{4,13}$ A, $v_t = 0$	447
233.79567	CH_3OH	$18_{3,15}$–$17_{4,14}$ A, $v_t = 0$	447
234.68337	CH_3OH	$4_{2,3}$–$5_{1,4}$ A, $v_t = 0$	61
236.93609	CH_3OH	$14_{1,13}$–$13_{2,12}$ A, $v_t = 0$	260
218.32479	HC_3N	24–23	131
236 512.79	HC_3N	26–25	153
217.10492	SiO	5–4	31
218.22219	H_2CO	$3_{0,3}$–$2_{0,2}$	21
219.56036	$C^{18}O$	2–1	16
220.17742	CH_2CO	$11_{1,11}$–$10_{1,10}$	76
220.39868	^{13}CO	2–1	16

Notes. The molecular data are taken from the Cologne Database for Molecular Spectroscopy (CDMS; Müller et al. 2001; Endres et al. 2016). Column 1 reports the rest frequency of the transition; column 2 the molecular species; column 3 the quantum numbers; column 4 the upper state energy. The quantum numbers are given depending on the symmetry of the molecule: $J^{\rm upper} - J^{\rm lower}$ for linear, $J_K^{\rm upper} - J_K^{\rm lower}$ for symmetric top, and $J_{K_a,K_c}^{\rm upper} - J_{K_a,K_c}^{\rm lower}$ for asymmetric top molecules.

distribution is traced with bright lines of CH_3CN, CH_3OH, HC_3N, and SO_2. While the 1.3 mm continuum is only slightly resolved in IRAS 21078+5211, in G035.02+0.35, at comparable linear resolution, it presents an extended structure approximately parallel to the disk midplane. In both regions, all the molecular lines trace a well-defined $V_{\rm LSR}$ gradient along the direction of the disk. Specifically for IRAS 21078+5211, a characteristic feature of all the velocity maps, although best visible in the SO emission, is the green strip that bisects the maps, forming a small angle with the jet axis (see Figs. 1 and 2). The most striking difference between the two YSOs is in regard to the elongation of the molecular emissions, which are parallel to the jet in IRAS 21078+5211 and to the disk in G035.02+0.35. In both targets, the emission of SO_2 is more compact than that of CH_3CN and CH_3OH, particularly in IRAS 21078+5211, where the latter covers a much wider area around the jet axis.

3.2. Physical conditions

To determine the physical conditions of the gas, we used the spectral analysis software Madrid Data Cube Analysis (MADCUBA[2]; Martín et al. 2019) to identify and fit the emission of several molecular species. For both IRAS 21078+5211 and G035.02+0.35, we derived the spectral emission in the direction of the YSO by integrating the signal over the area inside the lowest 1.3 mm continuum contour (the thick green contours in Figs. 2 and 3, respectively). In IRAS 21078+5211, since the molecular emission is significantly more extended than the 1.3 mm continuum, we also extracted spectra at two positions in the outflow: (1) along the outflow axis (inside the thick green square in Fig. 2 centered at RA(J2000) = $21^{\rm h}\,09^{\rm m}\,21\overset{\rm s}{.}691$ and Dec(J2000) = $+52^\circ\,22'\,36\overset{''}{.}76$, with size of $0\overset{''}{.}2$); (2) at a wide separation from the axis (inside the thick blue square in Fig. 2 centered at RA(J2000) = $21^{\rm h}\,09^{\rm m}\,21\overset{\rm s}{.}735$ and Dec(J2000) = $+52^\circ\,22'\,36\overset{''}{.}77$, with a size of $0\overset{''}{.}2$).

Using the SLIM (Spectral Line Identification and Modeling) tool of MADCUBA, we surveyed the spectra to search for molecular species with a relatively large number of unblended and optically thin lines suitable for deriving the gas physical conditions in the inner regions close to the YSO. We selected the CH_3CN, CH_3OH, and SO_2 molecules (see Table 3) that in both targets have optical depths of less (or much less) than 0.25, and cover a sufficiently wide range in excitation energy to allow for a reliable estimate of the excitation temperature. In IRAS 21078+5211, we fit the emission of SO and HC_3N, too, since, owing to the wider frequency coverage of the observational setup, multiple lines are observed for these molecules, too.

To derive the physical parameters of molecular gas, we used the tool AUTOFIT of MADCUBA, which compares the observed spectra with the LTE synthetic spectra, taking into account all transitions and the line opacities. We warn that a single component was fit for each molecular species, under the assumption of negligible density and temperature gradients. Leaving four parameters free to vary, that is, the column density ($N_{\rm col}$), excitation temperature ($T_{\rm ex}$), line $V_{\rm LSR}$ (v_0), and line width (FWHM), AUTOFIT provides the best nonlinear least-squares fit using the Levenberg-Marquardt algorithm (Levenberg 1944; Marquardt 1963). Nominal errors of the fit parameters were derived from the diagonal elements of the covariance matrix calculated at the χ^2 minimum. Figures A.1, A.2 and A.3 present the result of the fit for a subset of the more unblended and intense lines of each molecular species. The emission profile of each transition is reasonably well fit with MADCUBA, determining the values of the column density, temperature, velocity, and line width listed in Table 3.

[2] https://cab.inta-csic.es/madcuba/

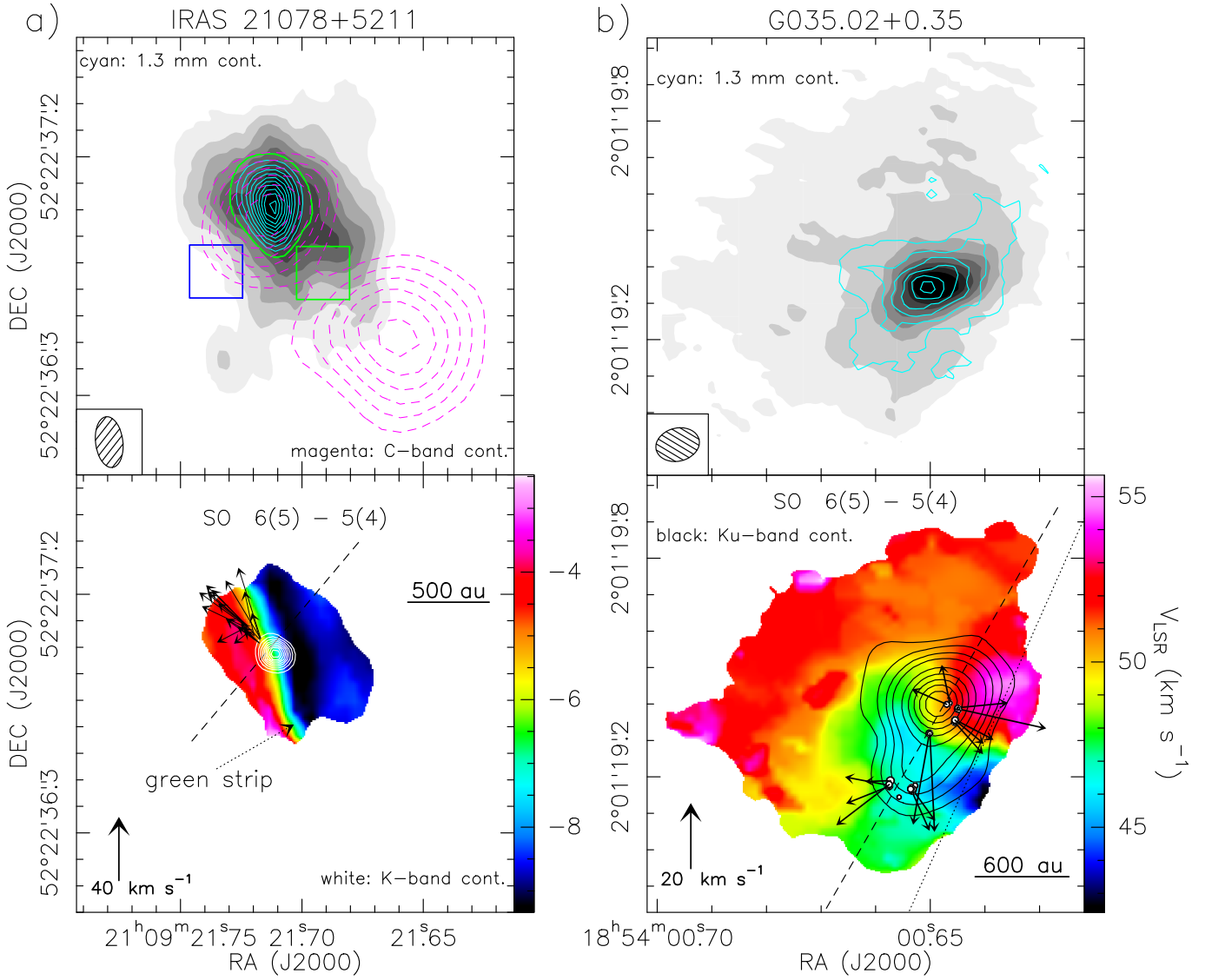

Fig. 1. Rotating wind in IRAS 21078+5211 (panel a) and G035.02+0.35 (panel b). In both panels, the grayscale and color maps in the upper and lower plots correspond to the velocity-integrated emission and intensity-weighted velocity, respectively, of the SO 6_5–5_4 line. The green color represents $V_{\rm LSR}$ close to the systemic velocity. (Panel a) The level contours of the grayscale filled-contours map in the upper plot are from 10 to 80% in steps of 10% of the map peak of 0.25 Jy beam^{-1} km s^{-1}. Cyan contours reproduce the 1.3 mm continuum showing levels from 1.9 to 11.9 mJy beam^{-1} at steps of 1.0 mJy beam^{-1}. The JVLA C- and K-band continuum emissions are given by magenta and white contours, respectively, and black arrows show the proper motions of the 22 GHz water masers (Moscadelli et al. 2016, see their Fig. 8). The dashed black line marks the direction of the disk midplane at PA≈140° (see Sect. 3.1). The thick green contour and thick green and blue squares in the upper plot delimitate the integration area for the spectra toward the YSO and outflow (see Sect. 3.2). In the lower plot, the green strip (see Sects. 3.1 and 4.1.1) is indicated. (Panel b) The level contours of the grayscale filled-contours map in the upper plot are 5%, 15%, and from 30 to 80% in steps of 10% of the map peak of 0.70 Jy beam^{-1} km s^{-1}. Cyan contours reproduce the 1.3 mm continuum showing levels from 1.2 to 6.2 mJy beam^{-1} at steps of 1.0 mJy beam^{-1}. The JVLA Ku-band continuum emission is shown with black contours, and black-edge white dots and black arrows give the positions and proper motions of the 22 GHz water masers (Moscadelli et al. 2019b, see their Fig. 2). The dashed black line marks the direction of the disk midplane at PA≈150° (see Sect. 3.1). The dotted black line crossing the loci of maximum and minimum $V_{\rm LSR}$ indicates the approximate direction of the SO $V_{\rm LSR}$ gradient.

4. Discussion

To study the gas kinematics, we constructed position-velocity (PV) plots of the molecular emissions along the YSO disk midplane (marked by the dashed black line in Figs. 1, 2 and 3). Before producing the PV plot, the emission was averaged across a beam in the direction perpendicular to the positional cut. Figures 4 and 5 show the PV plots of representative lines of SO, CH_3OH, CH_3CN, and SO_2 for IRAS 21078+5211 and G035.02+0.35, respectively.

4.1. Magneto-centrifugal winds

In a magneto-centrifugal wind, gas particles are launched along a streamline with a specific angular momentum higher than that of the gas in the disk. A general outcome of the models is that, along a given streamline, the rotational velocity of the wind, starting from the Keplerian value at the launch radius, stably grows till reaching the Alfvén point, then decreases beyond that point owing to the significant inertia of the flow, and finally increases again due to conservation of angular momentum when

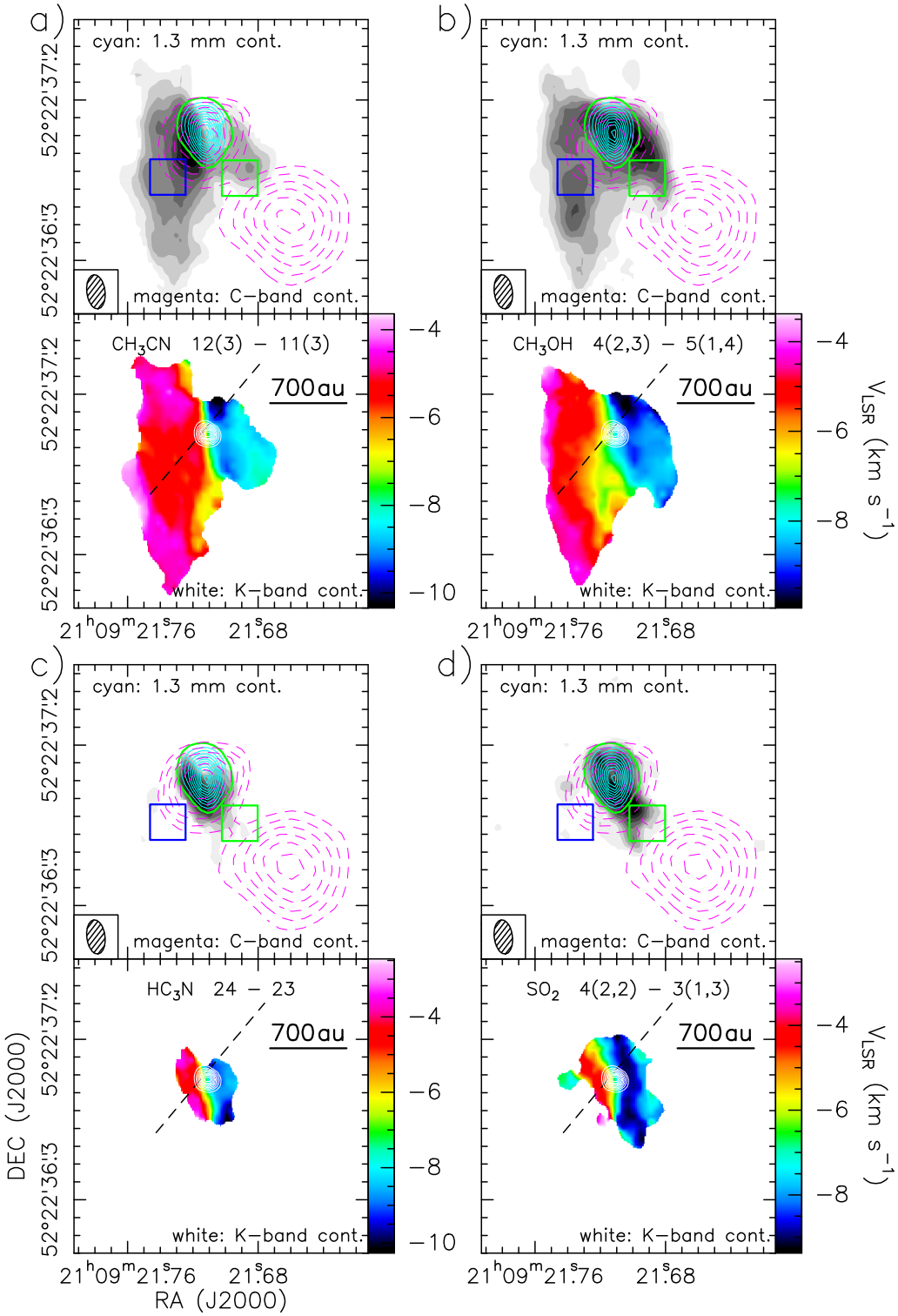

Fig. 2. Structure and kinematics of the IRAS 21078+5211 wind in molecular tracers. Each of the four panels presents the maps of the velocity-integrated emission (upper plot) and intensity-weighted velocity (lower plot) for a specific molecular line, as labeled. The level contours of the grayscale filled-contours maps in the upper plots are from 10 to 80% in steps of 10% of the map peak. Contours, lines, and symbols have the same meanings as in Fig. 1a.

the wind starts recollimating (see, e.g., Tabone et al. 2020). Based on this qualitative arguments, at distances of ∼100 au from the disk midplane of YSOs of ∼10 $M_{\odot}$, we can expect that a magneto-centrifugal wind displays a Keplerian rotation profile comparable to that of the gas rotating in the disk.

4.1.1. IRAS 21078+5211

In IRAS 21078+5211, all the molecular emissions are elongated in the direction of the jet and trace a common $V_{\rm LSR}$ gradient transversal to the jet axis. These two findings provide strong

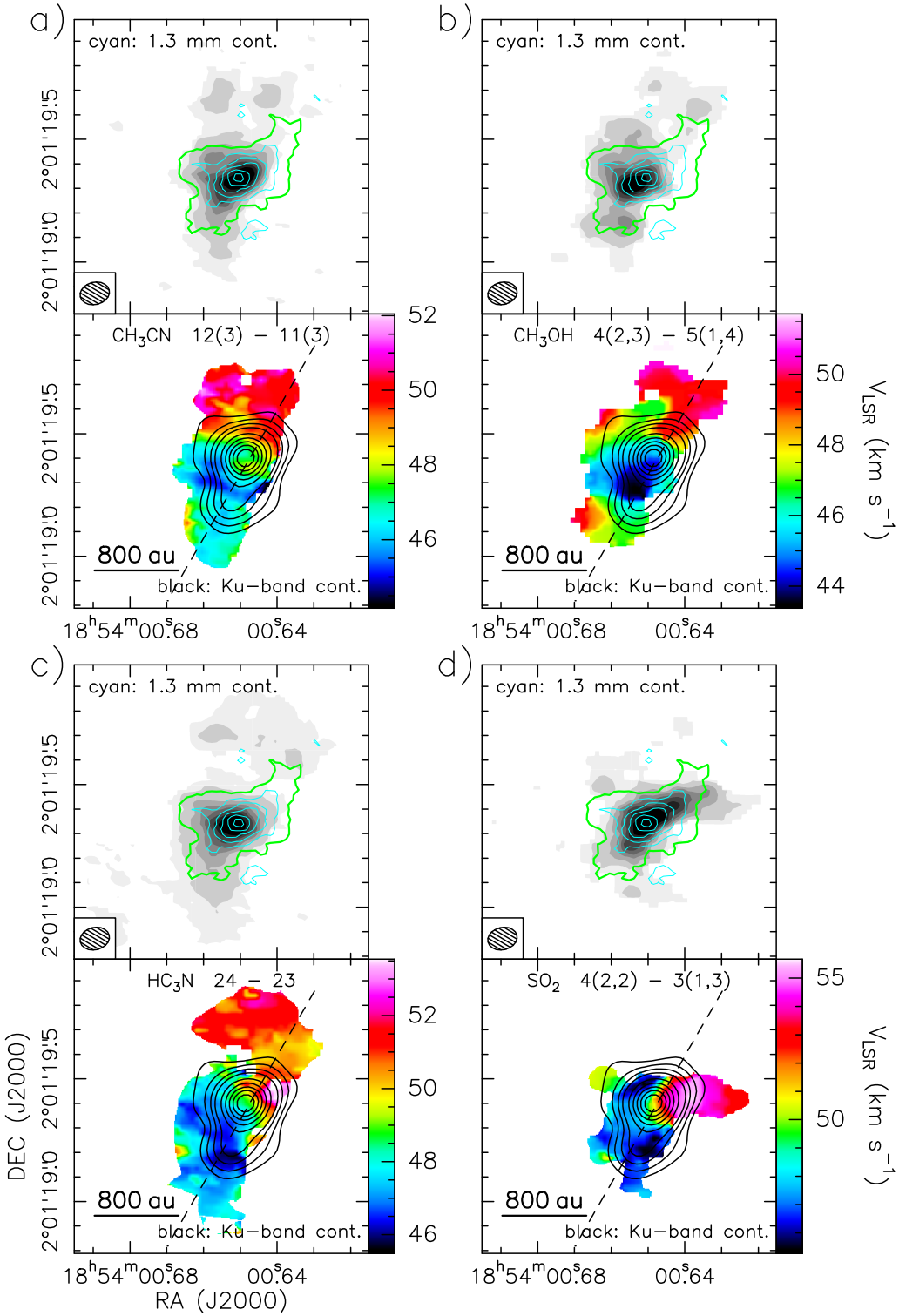

Fig. 3. Structure and kinematics of the G035.02+0.35 disk in molecular tracers. Each of the four panels presents the maps of the velocity-integrated emission (upper plot) and intensity-weighted velocity (lower plot) for a specific molecular line, as labeled. The level contours of the grayscale filled-contours maps in the upper plots are 5%, 15%, and from 30 to 80% in steps of 10% of the map peak. The thick green contour in the upper plots delimitates the integration area for the spectrum toward the YSO (see Sect. 3.2). Other contours and lines have the same meanings as in Fig. 1b.

evidence for a rotating wind emerging from the YSO. It is best traced by the emissions of SO (see Fig. 1a) and SO_2 (see Fig. 2d), which, being typical outflow tracers, present the best collimation along the jet axis. Besides, looking at Fig. 4, the SO velocity profile, which is one of the most extended in radius, shows the best indication of Keplerian rotation. The PV plots in Fig. 4 were obtained by averaging the emission perpendicularly to the disk midplane across a distance of ≈250 au much longer than the expected height of the disk atmosphere. If SO is mainly excited in the wind, its velocities should reliably trace the gas motion at the base of the wind. The contribution of the disk kinematics on the PV plot of SO in Fig. 4 can be evaluated by comparing it with

Table 3. Physical parameters from the fit of the molecular lines.

Species	T_{ex} (K)	N_{col} (10^{16} cm^{-2})	v_0 (km s^{-1})	FWHM (km s^{-1})	$\langle\tau\rangle$, τ_{max}
IRAS 21078+5211 YSO					
SO	33±3	1.3±0.4	−7.0±0.3	7.6±0.8	0.2, 5
SO_2	168±13	4.7±0.3	−6.8±0.2	9.0±0.5	0.08, 0.18
CH_3OH	217±7	43.4±1.6	−6.5±0.1	7.8±0.2	0.07, 0.23
CH_3CN	320±50	1.0±0.2	−6.9±0.2	9.3±0.5	0.05, 0.11
HC_3N	78±26	0.07±0.02	−6.3±0.3	10.8±0.7	0.17, 0.18
IRAS 21078+5211 Outflow					
Along the axis:					
SO	30±2	1.8±2.5	−7.0±0.2	3.6±0.8	0.1, 16
SO_2	132±25	1.6±0.2	−9.1±0.5	8.3±1.2	0.04, 0.10
CH_3OH	207±10	26.2±1.6	−8.6±0.1	5.6±0.3	0.03, 0.22
CH_3CN	165±29	0.19±0.05	−8.1±0.2	4.7±0.4	0.09, 0.21
HC_3N	43±29	0.05±0.07	−9.5±0.5	5.9±1.3	0.17, 0.20
Far from the axis:					
SO	18±2	1.2±0.9	−5.3±0.3	4.0±0.7	7.3, 15
SO_2	118±9	0.78±0.05	−6.4±0.1	4.4±0.3	0.04, 0.12
CH_3OH	216±7	34.8±1.4	−5.5±0.1	4.5±0.1	0.10, 0.33
CH_3CN	133±15	0.16±0.01	−5.5±0.1	3.8±0.2	0.13, 0.32
HC_3N	58±57	0.02±0.02	−5.7±0.6	6.0±1.5	0.07, 0.08
G035.02+0.35 YSO					
SO_2	145±5	12.5±0.6	49.6±0.3	12.2±0.6	0.11, 0.20
CH_3OH	257±10	68.9±4.1	45.4±0.1	5.7±0.2	0.11, 0.25
CH_3CN	470±56	2.1±0.2	46.6±0.1	6.7±0.3	0.06, 0.11

Notes. Results of the MADCUBA fits of the spectra extracted toward the YSO for both IRAS 21078+5211 and G035.02+0.35 and toward the outflow for IRAS 21078+5211 only (see Sect. 3.2). Column 1 reports the molecular species; columns 2–5 give, respectively, the excitation temperature, the column density, the velocity, and the line width of the fit molecular lines; column 6 lists the average and maximum optical depth of the fit molecular lines.

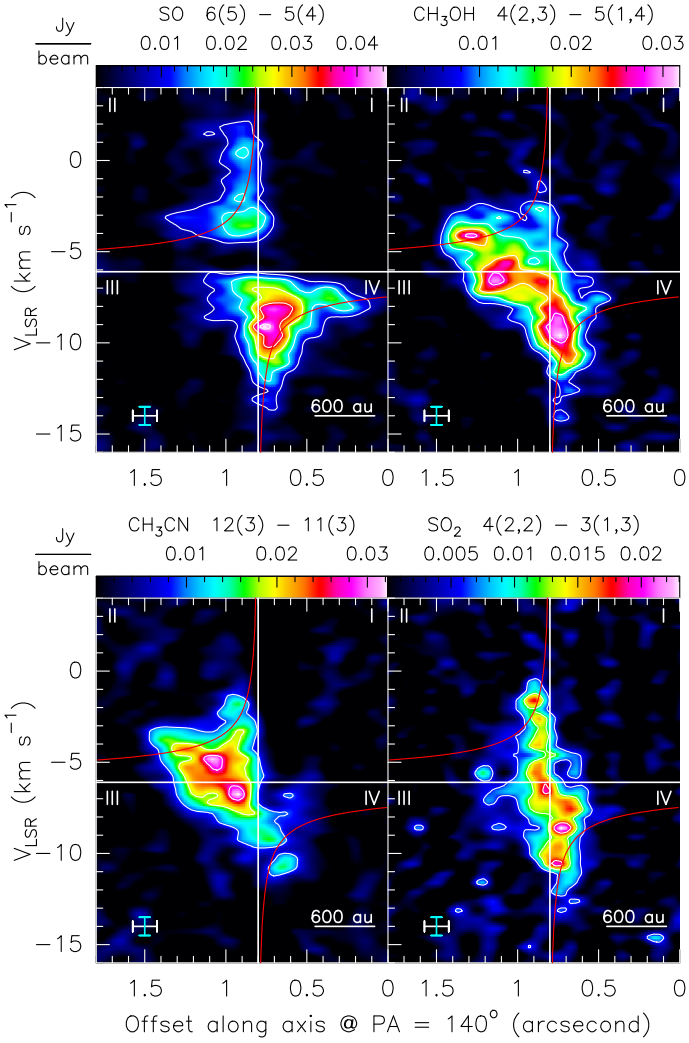

Fig. 4. Gas kinematics in IRAS 21078+5211. Each of the four panels presents the PV plot along the cut at PA = 140° (marked by the dashed black line in Figs. 1a and 2) of the molecular line specified above the panel. PV plots are shown with color maps and white contours, with contour levels ranging from $|I_{min}|/2$ to I_{max} at steps of $|I_{min}|/2$, where I_{min} and I_{max} are the minimum and maximum of the map, respectively. In each panel, the vertical and horizontal white axes denote the positional offset (≈0.″8) of the YSO relative to the phase center of the observations and YSO V_{LSR} (≈−6.1 km s^{-1}), respectively. The four quadrants are labeled with roman numbers. For comparison, the red curve shows the Keplerian velocity profile for a central mass of 6 $M_\odot$. In the lower left corner of the panels, the vertical cyan and horizontal white error bars indicate the velocity and spatial resolutions, respectively.

PV plots at positions along the jet axis sufficiently far from the disk midplane (see Fig. B.1) such that only the outflow motion can contribute. These off-disk PV plots show velocity profiles consistent with that at the disk midplane, confirming that the SO emission traces mainly the wind kinematics.

Comparing the PV plots of SO and SO_2, with respect to SO, SO_2 is emitted from gas projected on the sky closer to the jet axis, which probably reaches the highest (absolute) velocities at the smallest line-of-sight distances from the YSO. Ultimately, the kinematics traced by SO and SO_2 suggests a magneto-centrifugal launch of the wind, where the rotation velocities of the wind streamlines follow a Keplerian pattern similar to that of their launch radii in the disk.

We can reasonably rule out that the observed V_{LSR} gradient transversal to the jet axis is due to the rotation of the ambient gas induced by the gravitational force of the YSO. Let us indicate with Z (increasing to northeast) and R (increasing to northwest) the distances from the YSO measured along and across the jet axis. Assuming centrifugal equilibrium we can write

$$\frac{V_{rot}^2}{R} = F_g(Z,R) = \frac{G\,M}{Z^2+R^2}\,\frac{R}{\sqrt{Z^2+R^2}}, \quad (1)$$

where V_{rot} is the rotational velocity, M is the YSO mass, and $F_g(Z,R)$ is the gravitational force at the position (Z,R) corrected by the factor $R/\sqrt{Z^2+R^2}$ to take into account its inclination with respect to the rotation radius. From Eq. (1), the derivative of the rotational velocity with R is given by

$$\frac{dV_{rot}}{dR} \approx 0.95\,\frac{\sqrt{M}}{\sqrt{d}}\,\frac{Z^2-0.5\,R^2}{[Z^2+R^2]^{7/4}}, \quad (2)$$

where the rotation velocity, V_{rot}, is measured in kilometers per second, Z and R in arcseconds, and M and (the source distance) d are in solar mass and kiloparsecs. Let us consider the positions (Z_{gs},R_{gs}) along the green strip (see Sect. 3.1 and Fig. 1a, lower plot), where, for our choice of velocity-color code, the transversal V_{LSR} gradient is best visible. Along this strip we have $|Z_{gs}| > |R_{gs}|$ and $|Z_{gs}|^2 \gg |R_{gs}|^2$, such that we can approximate

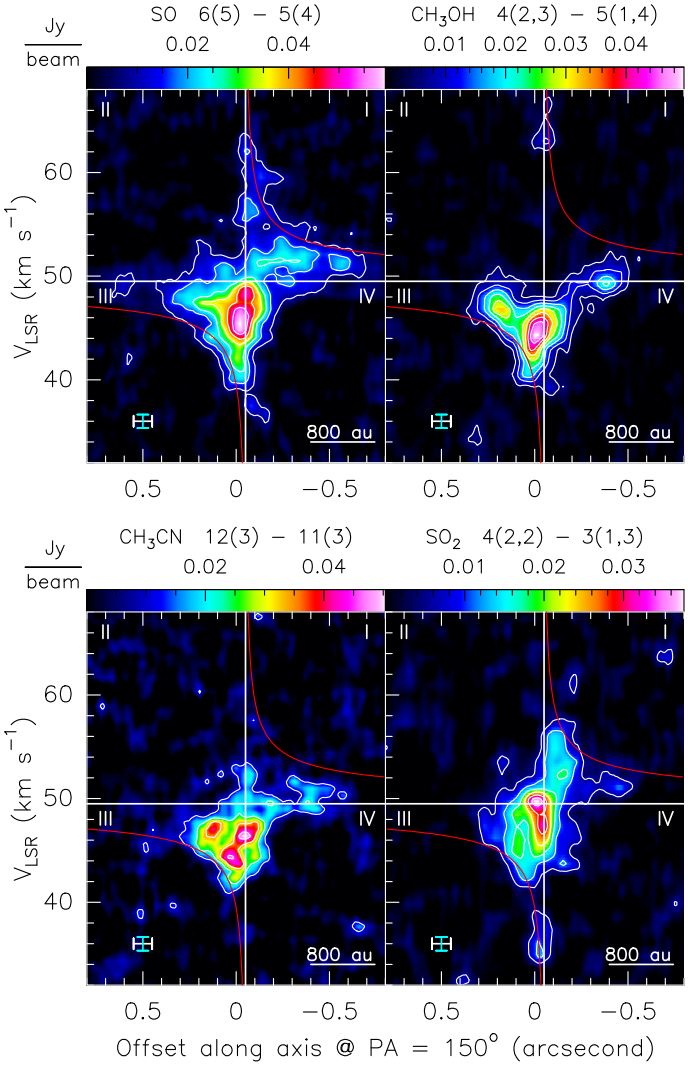

Fig. 5. Gas kinematics in G035.02+0.35. Each of the four panels presents the PV plot along the cut at PA = 150° (marked by the dashed black line in Figs. 1b and 3) of the molecular line specified above the panel. PV plots are shown with color maps and white contours, with contour levels ranging from $|I_{\rm min}|/2$ to $I_{\rm max}$ at steps of $|I_{\rm min}|/2$, where $I_{\rm min}$ and $I_{\rm max}$ are the minimum and maximum of the map, respectively. In each panel, the vertical and horizontal white axes denote the positional offset (≈−0.″05) of the YSO relative to the phase center of the observations and YSO $V_{\rm LSR}$ (≈49.5 km s^{-1}), respectively. The four quadrants are labeled with roman numbers. For comparison, the red curve shows the Keplerian velocity profile for a central mass of 20 $M_\odot$. In the lower left corner of the panels, the vertical cyan and horizontal white error bars indicate the velocity and spatial resolutions, respectively.

Eq. (2) with

$$\frac{{\rm d}V_{\rm rot}}{{\rm d}R} \approx 0.95\,\frac{\sqrt{M}}{\sqrt{d}}\,\left|Z_{\rm gs}\right|^{-3/2}. \qquad (3)$$

Across the green strip one observes $V_{\rm LSR}$ changes as large as $\Delta V_{\rm rot} \approx 6$ km s^{-1} over radial offsets as small as $\Delta R \approx 0.''2$ (see Fig. 1a, lower plot). Using these values in Eq. (3) to calculate the derivative ${\rm d}V_{\rm rot}/{\rm d}R$, at the extremes of the green strip where $\left|Z_{\rm gs}\right| \approx 0.''3$, we derive a value for the YSO mass, $M \approx 44\ M_\odot$. This value greatly exceeds the value of the YSO mass of 5.6±2 $M_\odot$ determined by studying the kinematics of the molecular lines tracing the disk rotation (Moscadelli et al. 2021). Therefore, we can conclude that the observed $V_{\rm LSR}$ gradient is by far too large to correspond to the rotation of the YSO envelope, and has to be linked instead with the rotation of the wind.

In the following we discuss the origin of the green strip that bisects the velocity maps of IRAS 21078+5211 (see Figs. 1a and 2). Since the green color represents the YSO $V_{\rm LSR}$ (≈−6.1 km s^{-1}), one can see that the $V_{\rm LSR}$ along the jet axis is redshifted to northeast and blueshifted to southwest. That agrees with the polarity of the SO outflow observed at larger scales (Moscadelli et al. 2021, see their Fig. 9). Thus, the straightforward interpretation of the tilt of the green strip with respect to the jet axis is that the jet is being accelerated at scales of ∼100 au, such that the $V_{\rm LSR}$ along the jet axis is progressively more redshifted (blueshifted) to northeast (southwest). The fact that the loci where the jet $V_{\rm LSR}$ equals that of the YSO are found (approximately) along a line might be explained assuming that the change of $V_{\rm LSR}$ is (approximately) linear for small displacements. At a given position, Z, along the axis, the jet acceleration causes a $V_{\rm LSR}$ variation from the systemic velocity $\Delta V_{\rm ax} = C_{\rm ax}\,Z$, with $C_{\rm ax}$ being a constant. Similarly, in the radial direction, the rotation produces a change from the axial $V_{\rm LSR}$, $\Delta V_{\rm rot} = C_{\rm rot}\,R$. At the positions $(Z_{\rm gs}, R_{\rm gs})$ of the green strip, $|\Delta V_{\rm ax}| = |\Delta V_{\rm rot}|$ and $R_{\rm gs}/Z_{\rm gs} = C_{\rm rot}/C_{\rm ax}$. The constant ratio between $R_{\rm gs}$ and $Z_{\rm gs}$ can explain the occurrence of the green strip.

4.1.2. G035.02+0.35

In G035.02+0.35, at scales of ≈1000 au, all the molecular lines (see Fig. 3), with the exception of SO (see Fig. 1b), have a flattened spatial distribution along the major axis of the disk, and their $V_{\rm LSR}$ gradients trace the disk rotation. We confirm the results of Beltrán et al. (2014), and the improvement in angular resolution (from ≈0.″4 to ≈0.″1) now allows the disk kinematics to be fully resolved. Figure 5 shows that all the molecular lines, and particularly the SO emission, present a Keplerian velocity profile. The archival data of G035.02+0.35 belong to the "Digging into the Interior of Hot Cores with ALMA" (DIHCA) project, a large program to study at high angular resolution the disk kinematics in ≈30 high-mass YSOs. Olguin et al. (2026) have recently completed the analysis of the gas kinematics for all the regions, and, specifically for G035.02+0.35, their fit of the Keplerian velocity profile of the CH_3CN emission yields a YSO mass of ≈20 $M_\odot$. This value is significantly higher than the previous estimate of 5–13 $M_\odot$ by Beltrán et al. (2014), which was probably affected by the insufficient angular resolution.

Figure 3 shows that the emissions of the molecular lines, dust, and free-free continuum are basically overlapping in the disk. That is certainly due to insufficient angular resolution to resolve the disk structure vertically, since ionized and neutral gas cannot be cospatial. This is also indicated by the fact that the emission peaks of the neutral components, i.e., molecular lines and dust, are slightly displaced with respect to that of the free-free continuum (see Fig. 3). It is natural to assume that the molecular gas and dust trace the disk midplane, while higher levels of ionization are expected in the disk atmosphere owing to both the stellar irradiation of energetic (mainly far-ultraviolet, FUV) photons (Gorti et al. 2015) and shocks from turbulent motions or the launch of a fast wind (Pascucci et al. 2023). Regarding this point, we note that the radio emission of G035.02+0.35 is orders of magnitude below the level expected from ionization by the Lyman continuum of a zero-age-main-sequence (ZAMS) star of corresponding bolometric luminosity (Sanna et al. 2018, 2019b), which favors shocks as the main

route of gas ionization. However, the high temperatures of 300–500 K of the molecular gas derived from the fit of the CH_3OH and CH_3CN lines (see Table 3) indicate that the disk is strongly heated by the stellar radiation and possibly even ionized at small radii.

The SO and SO_2 emissions in IRAS 21078+5211 and G035.02+0.35 share a number of common properties. In both YSOs, the SO emission extends well above and below the disk and presents the clearest Keplerian-like rotation profile (see Figs. 4a and 5a). As in IRAS 21078+5211, also in G035.02+0.35 the PV plots of SO across the disk midplane and offset of the disk (see Fig. B.2) are fully consistent with each other, which ensures that SO is tracing the rotation profile of the gas in the wind. In both YSOs, SO_2 emerges from gas seen in projection close to the disk rotation axis that yields the steepest profile of velocity with position (see Figs. 4d and 5d). Following the same reasonings as in Sect. 4.1.1, we propose that the SO and SO_2 emissions trace a magneto-centrifugal wind in G035.02+0.35, too. We provide further support to this hypothesis in Sect. 4.2.2.

4.2. X-wind versus disk wind

So far, we have discussed the evidence for magneto-centrifugally launched winds in IRAS 21078+5211 and G035.02+0.35, but we have not discriminated between the alternative scenarios of X-wind or DW. In the former case, the observed rotating molecular outflows should be ambient material entrained in a fast wide-angle X-wind launched at radii $\leq$0.1 au (López-Vázquez et al. 2019). In the latter case, the gas would be ejected directly from an extended portion, ~1–10 au, of the accretion disk.

4.2.1. IRAS 21078+5211

In IRAS 21078+5211 the emissions of CH_3CN and CH_3OH (see Fig. 2, panels a and b, respectively) wrap the radio jet inside a funnel-like pattern that is significantly wider than the longitudinal patterns of SO (see Fig. 1a), and HC_3N and SO_2 (see Fig. 2, panels c and d, respectively). In addition, the PV plots of CH_3CN and CH_3OH present elongated emission threading the second and fourth quadrants (see Fig. 4), which is consistent with a rotating ring. The latter could actually be the kinematic structure responsible for the emission of the two molecules, since all the corresponding lines are optically thin (see Table 3) and we would have seen the contribution of gas inside the rings otherwise.

Besides the diverse radial extension, there are also clear differences present in the structure of the molecular emissions. While the emissions of SO, HC_3N, and SO_2 are rather homogeneous, those of CH_3CN and CH_3OH are irregular and concentrated in a few blobs with sizes of 500–1000 au (see Fig. 2). All these molecular species are mainly excited in the YSO wind, as one can infer comparing the physical conditions derived at the positions of the YSO and outflow (see Table 3). Except for CH_3CN, which certainly has a contribution from the denser and warmer disk gas toward the YSO, all the other molecules have comparable values for the excitation temperature and, in some cases, the column density, too, between the YSO and outflow positions. If the molecular emissions arise in shocks of the protostellar wind, the different structures can be explained by the varying nature of the shocks. The wider and irregular intensity distributions of CH_3CN and CH_3OH can be produced by a discrete number of relatively large (exceeding the beam size of 250 au) and strong, external shocks of the wind against dense clumps of the surrounding medium. The homogeneous emissions of SO, HC_3N, and SO_2 can result from a higher number of smaller (~10–100 au) weaker internal shocks.

High abundances of CH_3OH are expected in the post-shock layers of C-type shocks for shock velocity $V_s \gtrsim 12$ km s^{-1} sufficiently high for efficient sputtering of the CH_3OH molecules off the icy mantle of dust grains (Burkhardt et al. 2019; Baijot et al. 2026). For a pre-shock hydrogen number density, n_H, of 10^5–10^6 cm^{-3}, C-type shocks yield post-shock depths of warm molecular gas of ≈500–5000 au (see, e.g., Pineau des Forets et al. 1993), comparable with or larger than the irregular features observed in the CH_3CN and CH_3OH maps. Our excitation analysis confirms that the CH_3OH column density in the emission blobs far from the outflow axis is higher than along the outflow axis (see Table 3), despite the total gas density is expected to diminish with radius. It is also notable that the CH_3CN column density keeps about the same close and far from the outflow axis, while that of SO and SO_2 decreases from small to large radii.

On the other hand, the recent calculations by van Gelder et al. (2021), accounting for both warm gas-phase chemistry and thermal desorption from dust grains, show that 10–100 au layers of enhanced SO and SO_2 abundance can be produced behind J- and CJ-type shocks propagating across an high-density, $n_H \sim 10^7$ cm^{-3}, medium at a relatively low velocity, $V_s \approx 1-10$ km s^{-1}. In particular, the enhancement of SO_2 is predicted to occur only for the upper range of shock velocities, $V_s \approx 5-10$ km s^{-1}. In these shocks, while the gas reaches temperatures of a few thousand Kelvin at which more complex molecules (such as CH_3CN and CH_3OH) dissociate, the dust temperature, owing to efficient radiative cooling, stays lower than 70 K. Sublimation from the grain mantles of SO (at ≈37 K) and SO_2 (at ≈62 K) ices can occur, but not that of CH_3OH and H_2O ices requiring dust temperatures of 85–100 K (Suutarinen et al. 2014).

The above comparison with shock models supports our interpretation of the spatial distribution and structure of the CH_3OH and SO and SO_2 emissions in IRAS 21078+5211 in terms of large external and small internal shocks of the protostellar wind, respectively. Then, only a fraction of the observed CH_3OH (and CH_3CN) can possibly correspond to ambient material entrained in the external shocks of the wind, but the inner gas traced by SO and SO_2 can stem directly from the disk, endorsing the case of a MHD DW.

It is also interesting to note that the models by van Gelder et al. (2021) require higher shock velocities for the formation of SO_2 with respect to SO. That agrees very well with the MHD DW interpretation, where the gas traced by SO_2, closer to the jet axis, is predicted to move faster than that emitting SO. Therefore, it is also natural to expect that the internal shocks of the flow producing SO_2 have higher velocities than those of SO. Following the same reasoning, at sufficiently large radii, the velocity of MHD DWs and corresponding internal shocks would become too low ($\leq$1 km s^{-1}) for efficient production of SO, determining a maximum radius for the SO emission to be one of the preferential molecular tracers of DWs. Our analysis of the physical conditions supports both the models by van Gelder et al. (2021) and the MHD DW interpretation, since the excitation temperature of SO_2 is found to be systematically higher than that of SO at all the explored positions (see Table 3), in agreement with production in stronger shocks, and the continuous decrease in the SO_2 column density from near the YSO through small to large radii (see Table 3) clearly indicates its higher concentration in faster gas closer to the outflow axis.

So far we have considered the case that the observed molecular emissions are mainly determined by processes in the local shocks of the wind, but, alternatively, they could mainly reflect

the properties of the original gas of the primary wind. The radial distribution of the molecular emissions in IRAS 21078+5211 is reminiscent of what is found in low-mass YSOs, where, in an increasing number of cases, combined James Webb Space Telescope (JWST) and ALMA observations are now discovering fast collimated [Fe II] jets lying inside a hollow cavity delimited by wider and slower H_2 emission, which is itself nested inside a still wider and slower CO wind (Federman et al. 2024; Tychoniec et al. 2024; Pascucci et al. 2025). Such a nested morphology in velocity and chemistry of rotating winds at scales of a few hundred astronomical units is a distinctive characteristic of radially extended MHD DWs, in low-mass YSOs, at least, since it is very difficult to explain this as the result of gas entrainment (López-Vázquez et al. 2019; de Valon et al. 2022).

4.2.2. G035.02+0.35

In G035.02+0.35 the protostellar wind is traced by SO emission only. That already rules out the possibility that we are observing ambient gas entrained in a fast wide-angle X-wind as there is no reasonable explanation why all the other observed molecular emissions would not be present in the wind. However, before concluding in favor of a MHD DW, we need also to discuss the reason for the absence of these emissions if the wind material arises directly from the YSO disk.

As is pointed out in Sect. 1, the water maser 3D velocities appear to trace a rotating wind emerging from the disk. The high maser velocities, $\geq$20 km s^{-1}, favor a MHD DW rather than a photoevaporated DW, whose typical speeds are $\leq$10 km s^{-1} (Hollenbach et al. 1994; Alexander et al. 2014). Figure 1b (lower plot) shows that most of the water masers are found near the peaks of the free-free continuum emission. Since water masers are typical shock tracers on scales of 1–10 au (Hollenbach et al. 2013), that reinforces the interpretation of the free-free continuum in terms of shock ionization. The radio continuum, comparable in size to the elongation of the water maser distribution, could trace the launch region of the protostellar wind, the water masers marking strong ionizing shocks of the wind against dense static parcels of ambient gas.

Magnetohydrodynamic disk winds are launched from the disk atmosphere (Pudritz et al. 2007), which could be found at significantly higher temperature than the disk midplane. The temperature of the neutral gas of 300–500 K at radii of a few hundred astronomical units measured through the CH_3CN and CH_3OH lines (see Table 3) is in good agreement with predictions of the most recent simulations of high-mass YSOs, which also consider radiation forces and photo-ionization feedback (Kuiper & Hosokawa 2018, see their Fig. 6). If the disk atmosphere were heated by the energetic stellar photons of a $\approx$20 $M_\odot$ star, its temperature would be 10^3–10^4 K, as indicated by models of photo-ionization of massive disks (Hollenbach et al. 1994; Yorke & Welz 1996). In this specific case, the presence of an extended region of photo-ionized gas is unlikely, since the radio emission is orders of magnitude below the Lyman continuum level. The star could be in a bloating phase (Hosokawa & Omukai 2009; Hosokawa et al. 2016), predicted to occur within the range of YSO mass of 10–30 $M_\odot$ (Kuiper & Yorke 2013; Kuiper & Hosokawa 2018) and effectively observed for a $\approx$25 $M_\odot$ YSO (Pandey et al. 2025), and its photospheric temperature could be too low to emit ionizing photons.

In G035.02+0.35, however, there is a strong observational evidence that the disk surface is shock-ionized. Therefore, it is plausible to assume that the disk atmosphere is sufficiently warm over the DW launch region for the molecular gas to be partially or fully dissociated. The dust, instead, owing to efficient radiative cooling, could still retain temperatures of a few tens of Kelvin. That could explain the lack of molecular emissions other than SO in the DW. We note that the SO gas-phase formation in J-type shocks requires only the presence of dust in the pre-shock gas, as all the relevant molecular reactants are directly obtained through desorption from the icy dust mantles (van Gelder et al. 2021).

The SO_2 emission in G035.02+0.35 presents a compact arched structure contiguous to the disk (see Fig. 3d). That leads us to suppose that it could trace the base of the cavity of the DW and be excited in relatively strong shocks of the DW against the surrounding dense, likely infalling, gas. A similar interpretation holds also for the X-shape structure traced by the SO_2 emission that emerges from the rotating disk in G011.92−0.61 (Bayandina et al. 2025, see their Figs. 2 and 9).

In G035.02+0.35, the lack of SO_2 in the DW at larger distances from the disk and close to the jet axis, as is instead observed in IRAS 21078+5211, could still be linked with the paucity of the ultraviolet (UV) flux from the bloated star. In fact, the gas-phase formation of SO and SO_2 in J-shocks crucially depends on the strength of the local UV radiation field for the production of essential reactants via the photo-dissociation of H_2O, H_2S, and CH_4 (van Gelder et al. 2021). Models of massive star formation predict that the radiation from the star is preferentially beamed along the optically thin bipolar-outflow cavity (Krumholz et al. 2005; Kuiper et al. 2010), which in IRAS 21078+5211 could account for a sufficiently high UV-radiation flux close to the jet axis to form SO_2. On the other hand, if the source of ionization are exclusively shocks over the disk surface, one can expect that the diffuse UV radiation can affect only the DW gas closer to the disk, in agreement with the observed spatial distribution of the SO emission (see Fig. 1b, upper plot), and is absorbed before reaching the high-velocity shocks along the jet axis.

5. Conclusions

The POETS survey has investigated the launch region of protostellar outflows from luminous YSOs at scales of 10–100 au through VLBI observations of the water masers, finding good evidence for MHD DWs. Considering the fundamental role that MHD DWs could have in driving disk accretion and evolution, it is necessary to further test their presence and characterize their properties with complementary high-resolution millimeter interferometric observations. In our previous study of the POETS target G011.92−0.61 (Bayandina et al. 2025), the MHD DW interpretation based on water maser 3D velocities has been fully confirmed via sensitive ALMA observations at a linear resolution of $\approx$100 au. In this article, we have focused on the YSOs IRAS 21078+5211 and G035.02+0.35, two POETS targets of different mass, 5.6±2 and $\approx$20 $M_\odot$, respectively, associated with characteristic maser MHD DW configurations. We have investigated the base of the protostellar outflows at scales of 100–1000 au in these two YSOs using the same molecular lines at comparable linear and velocity resolutions and sensitivity.

In both YSOs, all the molecular emissions trace a clear V_{LSR} gradient transversal to the disk rotation (and, in IRAS 21078+5211, the radio jet) axis. Inspecting the PV plots across the disk midplane, in both sources, the SO emission is one of the most radially extended and presents the clearest Keplerian-like velocity profile, while SO_2 is spatially compact and yields

the steepest velocity-position profile. Our analysis of these kinematic findings supports the case of a wind magneto-centrifugally launched from the YSO disk.

The wind in IRAS 21078+5211 harbors many molecules with a clear radial distribution, going from SO_2 and HC_3N, found close to the jet axis, through SO, covering larger radii, to CH_3CN and CH_3OH, with the maximum width. In G035.02+0.35, only SO traces the wind, while the other molecular emissions are confined inside the disk. That already excludes the possibility of a X-wind, i.e., that the wind gas is entrained from the surrounding medium, as we should see other molecules, as well. Instead, if we are observing MHD DWs, i.e., if the wind gas is ejected directly from the disk, models of molecule production in shocks can explain both the radial distribution of molecular emissions in the protostellar wind of IRAS 21078+5211 and the absence of molecules, other than SO, in the G035.02+0.35's wind. The latter is a consequence of the fact that the launch region of the wind in the disk atmosphere is shock-ionized and the molecular gas is likely partially or fully dissociated.

The results obtained in IRAS 21078+5211 and G035.02+0.35, for two YSOs of significantly different mass, confirm the POETS conclusion that MHD DWs can be the common launching mechanism of protostellar winds in luminous YSOs. The gas kinematics traced by water masers at scales of 10–100 au and determined via thermal molecular lines at scales of 100–1000 au are very consistent. Considering also our recent findings in G011.92−0.61, we expect that SO and SO_2 emissions can be among the preferential tracers of MHD DWs in intermediate- and high-mass YSOs at small scales.

Acknowledgements. A.P. acknowledges financial support from the UNAM-PAPIIT IN120226 grant, and the Sistema Nacional de Investigadores of SECIHTI, México. A.S.-M. acknowledges support from the PID2023-146675NB grant funded by MCIN/AEI/10.13039/501100011033, and by the Spanish program Unidad de Excelencia María de Maeztu CEX2020-001058-M, financed by MCIN/AEI/10.13039/501100011033, and by the MaX-CSIC Excellence Award MaX4-SOMMA-ICE. D.S. was funded by the Deutsche Forschungsgemeinschaft (DFG, German Research Foundation) – project number: 550639632. R.E.P. is supported by a Discovery Grant from the National Science and Engineering Research Council (NSERC) of Canada. R.K. acknowledges financial support via the Heisenberg Research Grant funded by the Deutsche Forschungsgemeinschaft (DFG, German Research Foundation) under grant no. KU 2849/9, project no. 445783058.

References

Ahmadi, A., Beuther, H., Bosco, F., et al. 2023, A&A, 677, A171
Alexander, R., Pascucci, I., Andrews, S., Armitage, P., & Cieza, L. 2014, in Protostars and Planets VI, eds. H. Beuther, R. S. Klessen, C. P. Dullemond, & T. Henning (Tucson: University of Arizona Press), 475
Baijot, C., Groyne, M., & De Becker, M. 2026, A&A, 705, A185
Bayandina, O. S., Moscadelli, L., Cesaroni, R., et al. 2025, A&A, 694, A92
Beltrán, M. T., Cesaroni, R., Neri, R., et al. 2004, ApJ, 601, L187
Beltrán, M. T., Sánchez-Monge, Á., Cesaroni, R., et al. 2014, A&A, 571, A52
Beuther, H., Mottram, J. C., Ahmadi, A., et al. 2018, A&A, 617, A100
Blandford, R. D., & Payne, D. G. 1982, MNRAS, 199, 883
Briggs, D. S. 1995, BAAS, 27, 1444
Burkhardt, A. M., Shingledecker, C. N., Le Gal, R., et al. 2019, ApJ, 881, 32
CASA Team, Bean, B., Bhatnagar, S., et al. 2022, PASP, 134, 114501
Cesaroni, R., Felli, M., Jenness, T., et al. 1999, A&A, 345, 949
De Simone, M., Podio, L., Chahine, L., et al. 2024, A&A, 686, L13
de Valon, A., Dougados, C., Cabrit, S., et al. 2022, A&A, 668, A78
Endres, C. P., Schlemmer, S., Schilke, P., Stutzki, J., & Müller, H. S. P. 2016, J. Mol. Spectr., 327, 95
Federman, S. A., Megeath, S. T., Rubinstein, A. E., et al. 2024, ApJ, 966, 41
Gieser, C., Beuther, H., Semenov, D., et al. 2021, A&A, 648, A66
Gorti, U., Hollenbach, D., & Dullemond, C. P. 2015, ApJ, 804, 29
Högbom, J. A. 1974, A&AS, 15, 417
Hollenbach, D., Johnstone, D., Lizano, S., & Shu, F. 1994, ApJ, 428, 654
Hollenbach, D., Elitzur, M., & McKee, C. F. 2013, ApJ, 773, 70
Hosokawa, T., & Omukai, K. 2009, ApJ, 691, 823
Hosokawa, T., Hirano, S., Kuiper, R., et al. 2016, ApJ, 824, 119
Kadam, K., Vorobyov, E., Woitke, P., Basu, S., & van Terwisga, S. 2025, A&A, 695, A167
Königl, A., & Pudritz, R. E. 2000, Protostars and Planets IV (Tucson: University of Arizona Press), 759
Krumholz, M. R., McKee, C. F., & Klein, R. I. 2005, ApJ, 618, L33
Kuiper, R., & Hosokawa, T. 2018, A&A, 616, A101
Kuiper, R., & Yorke, H. W. 2013, ApJ, 763, 104
Kuiper, R., Klahr, H., Beuther, H., & Henning, T. 2010, ApJ, 722, 1556
Levenberg, K. 1944, Quarterly Appl. Math., 2, 64
López-Vázquez, J. A., Cantó, J., & Lizano, S. 2019, ApJ, 879, 42
Lynden-Bell, D., & Pringle, J. E. 1974, MNRAS, 168, 603
Marquardt, D. 1963, J. Soc. Industrial Appl. Math., 11, 431
Martín, S., Martín-Pintado, J., Blanco-Sánchez, C., et al. 2019, A&A, 631, A159
Moscadelli, L., Goddi, C., Cesaroni, R., Beltrán, M. T., & Furuya, R. S. 2007, A&A, 472, 867
Moscadelli, L., Cesaroni, R., Rioja, M. J., Dodson, R., & Reid, M. J. 2011, A&A, 526, A66
Moscadelli, L., Sánchez-Monge, Á., Goddi, C., et al. 2016, A&A, 585, A71
Moscadelli, L., Sanna, A., Cesaroni, R., et al. 2019a, A&A, 622, A206
Moscadelli, L., Sanna, A., Goddi, C., et al. 2019b, A&A, 631, A74
Moscadelli, L., Beuther, H., Ahmadi, A., et al. 2021, A&A, 647, A114
Moscadelli, L., Sanna, A., Beuther, H., Oliva, A., & Kuiper, R. 2022, Nat. Astron., 6, 1068
Moscadelli, L., Oliva, A., Sanna, A., Surcis, G., & Bayandina, O. 2024, A&A, 690, A81
Müller, H. S. P., Thorwirth, S., Roth, D. A., & Winnewisser, G. 2001, A&A, 370, L49
Narang, M., Tyagi, H., Ohashi, N., et al. 2026, ApJ, 1000, 184
Olguin, F. A., Sanhueza, P., Oya, Y., et al. 2026, ApJ, 999, 106
Pandey, R., Palau, A., Serna, J., et al. 2025, MNRAS, 541, 3772
Pascucci, I., Cabrit, S., Edwards, S., et al. 2023, ASP Conf. Ser., 534, 567
Pascucci, I., Beck, T. L., Cabrit, S., et al. 2025, Nat. Astron., 9, 81
Pelletier, G., & Pudritz, R. E. 1992, ApJ, 394, 117
Pineau des Forets, G., Roueff, E., Schilke, P., & Flower, D. R. 1993, MNRAS, 262, 915
Pudritz, R. E., Ouyed, R., Fendt, C., & Brandenburg, A. 2007, in Protostars and Planets V, eds. B. Reipurth, D. Jewitt, & K. Keil (Tucson: University of Arizona Press), 277
Pudritz, R. E., Cridland, A. J., Inglis, J., & Alessi, M. 2025, arXiv e-prints [arXiv:2505.22724]
Sánchez-Monge, Á., Schilke, P., Ginsburg, A., Cesaroni, R., & Schmiedeke, A. 2018, A&A, 609, A101
Sanna, A., Moscadelli, L., Cesaroni, R., et al. 2010, A&A, 517, A78
Sanna, A., Moscadelli, L., Goddi, C., Krishnan, V., & Massi, F. 2018, A&A, 619, A107
Sanna, A., Kölligan, A., Moscadelli, L., et al. 2019a, A&A, 623, A77
Sanna, A., Moscadelli, L., Goddi, C., et al. 2019b, A&A, 623, L3
Shakura, N. I., & Sunyaev, R. A. 1973, A&A, 24, 337
Shu, F., Najita, J., Ostriker, E., et al. 1994, ApJ, 429, 781
Suutarinen, A. N., Kristensen, L. E., Mottram, J. C., Fraser, H. J., & van Dishoeck, E. F. 2014, MNRAS, 440, 1844
Tabone, B., Cabrit, S., Bianchi, E., et al. 2017, A&A, 607, L6
Tabone, B., Cabrit, S., Pineau des Forêts, G., et al. 2020, A&A, 640, A82
Tychoniec, Ł., van Gelder, M. L., van Dishoeck, E. F., et al. 2024, A&A, 687, A36
van Gelder, M. L., Tabone, B., van Dishoeck, E. F., & Godard, B. 2021, A&A, 653, A159
Wu, Y. W., Sato, M., Reid, M. J., et al. 2014, A&A, 566, A17
Xu, Y., Li, J. J., Reid, M. J., et al. 2013, ApJ, 769, 15
Yorke, H. W., & Welz, A. 1996, A&A, 315, 555

Appendix A: Fit of the molecular emission

For each source, position and molecule reported in Table 3, we have identified and fit with MADCUBA all the unblended transitions within the observed frequency range. The result of the fit for a subset of the more unblended and intense lines of each molecular species is presented in Figs. A.1, A.2, and A.3.

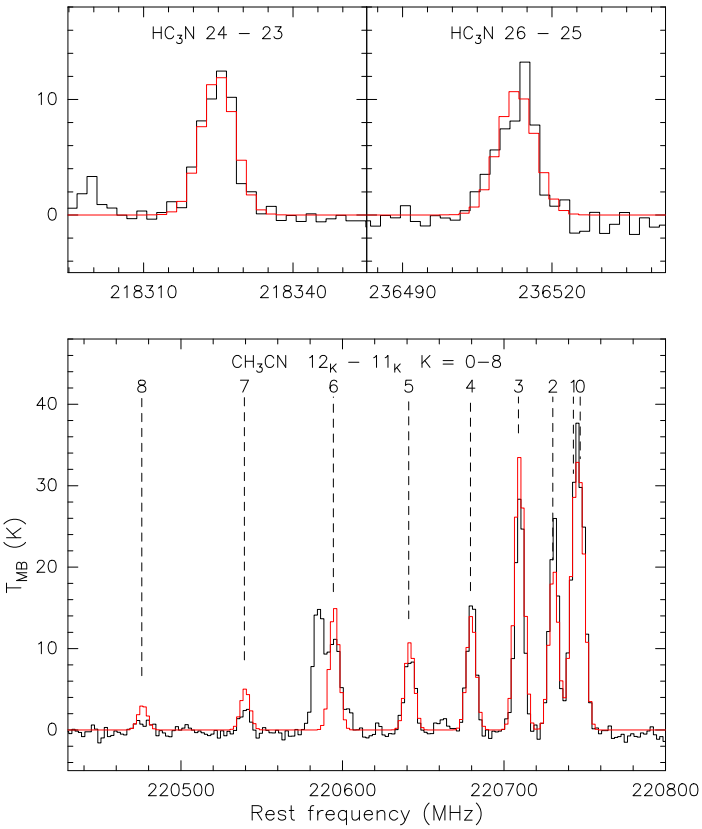

Fig. A.1: Fit of the molecular emission in IRAS 21078+5211. Each panel shows the observed (black) and fit (red) spectrum for a single or multiple molecular transitions, as labeled. Panels that refer to the same molecular species are grouped together.

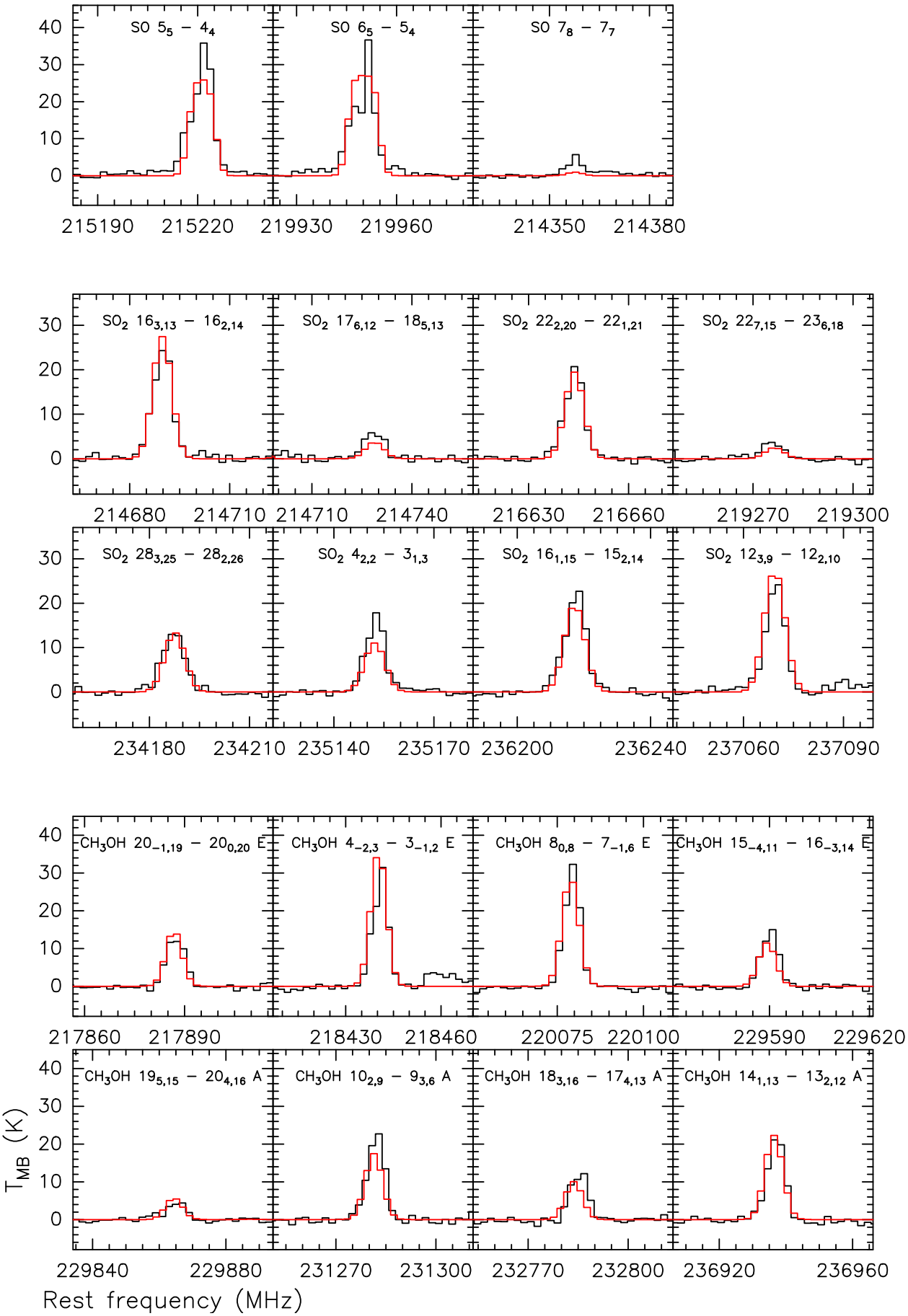

Fig. A.2: Same as for Fig. A.1.

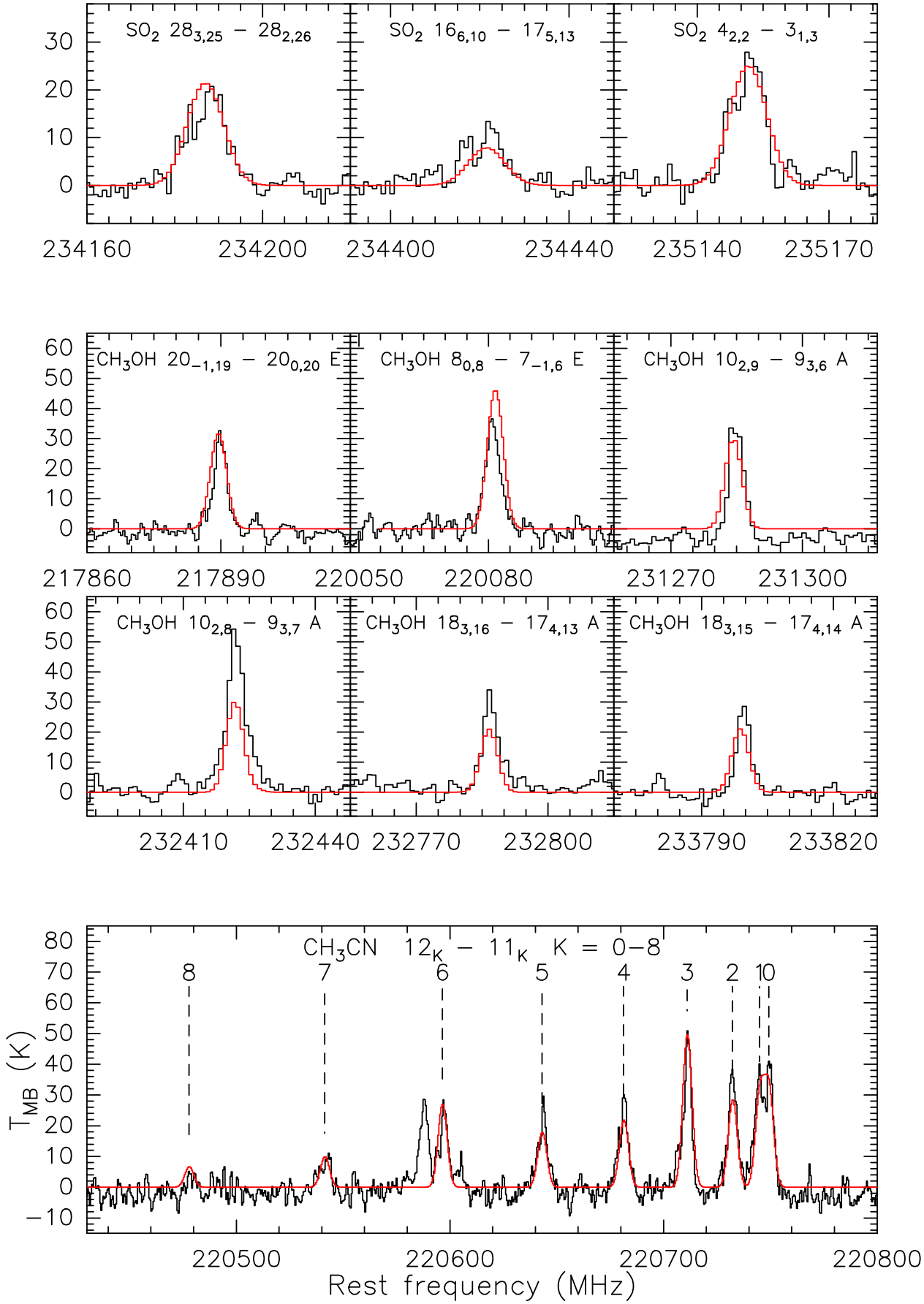

Fig. A.3: Fit of the molecular emission in G035.02+0.35. Each panel shows the observed (black) and fit (red) spectrum for a single or multiple molecular transitions, as labeled. Panels that refer to the same molecular species are grouped together.

Appendix B: PV plots of the SO emission along the disk rotation axis

Figures B.1 and B.2 report the PV plots of the SO 6_5–5_4 line at positions along the disk rotation axis above (northeast) and below (southwest) the disk midplane for IRAS 21078+5211 and G035.02+0.35, respectively.

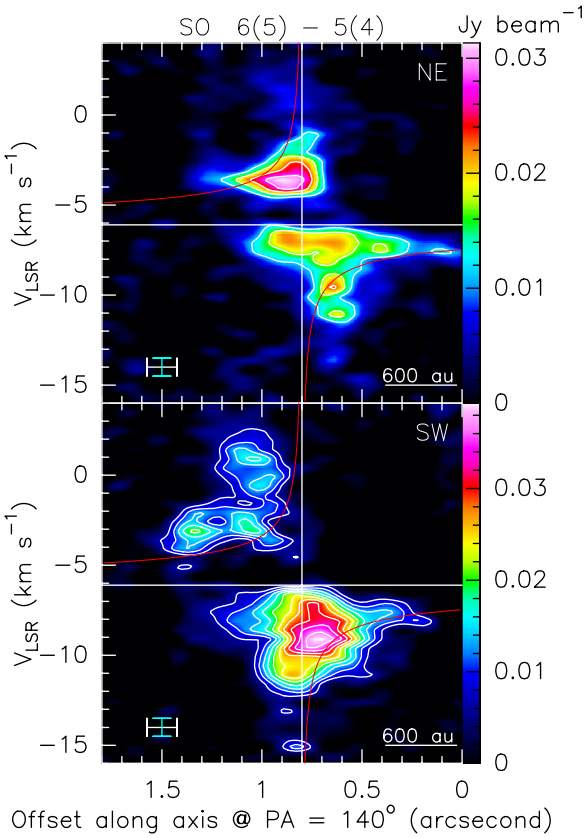

Fig. B.1: PV plots of the SO emission in IRAS 21078+5211 at positions offset from the disk midplane. The upper and lower panels present the PV plots of the SO 6_5–5_4 line along the direction at PA = 140° (marked by the dashed black line in Figs. 1 and 2) at positions along the disk rotation axis 0.″2 (i.e., the beam major axis) above (northeast) and 0.″2 below (southwest) the disk midplane, respectively. PV plots are shown with color maps and white contours, with contour levels ranging from $|I_{\rm min}|/2$ to $I_{\rm max}$ at steps of $|I_{\rm min}|/4$, where $I_{\rm min}$ and $I_{\rm max}$ are the minimum and maximum of the map, respectively. In each panel, the vertical and horizontal white axes denote the positional offset (≈ 0.″8) of the YSO relative to the phase center of the observations and YSO $V_{\rm LSR}$ (≈ −6.1 km s^{-1}), respectively. For comparison, the red curve shows the Keplerian velocity profile for a central mass of 6 $M_\odot$. In the lower left corner of the panels, the vertical cyan and horizontal white error bars indicate the velocity and spatial resolutions, respectively.

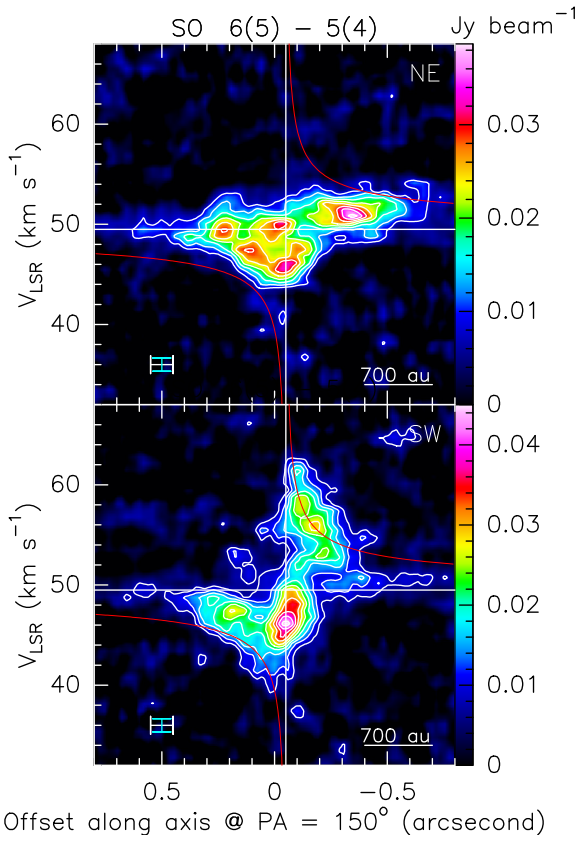

Fig. B.2: PV plots of the SO emission in G035.02+0.35 at positions offset from the disk midplane. The upper and lower panels present the PV plots of the SO 6_5–5_4 line along the direction at PA = 150° (marked by the dashed black line in Figs. 1 and 3) at positions along the disk rotation axis 0.″12 (i.e., the beam major axis) above (northeast) and 0.″12 below (southwest) the disk midplane, respectively. PV plots are shown with color maps and white contours, with contour levels ranging from $|I_{\rm min}|/2$ to $I_{\rm max}$ at steps of $|I_{\rm min}|/4$, where $I_{\rm min}$ and $I_{\rm max}$ are the minimum and maximum of the map, respectively. In each panel, the vertical and horizontal white axes denote the positional offset (≈ −0.″05) of the YSO relative to the phase center of the observations and YSO $V_{\rm LSR}$ (≈ 49.5 km s^{-1}), respectively. For comparison, the red curve shows the Keplerian velocity profile for a central mass of 20 $M_\odot$. In the lower left corner of the panels, the vertical cyan and horizontal white error bars indicate the velocity and spatial resolutions, respectively.